








Detection of Dust in High-velocity Cloud Complex C–Enriched Gas Accreting onto the Milky Way*

Andrew J. Fox^{1,2} , Frances H. Cashman³ , Gerard A. Kriss³ , Gisella de Rosa³ , Rachel Plesha³ ,
Yasaman Homayouni^{3,4,5} , and Philipp Richter⁶ 

¹ AURA for ESA, Space Telescope Science Institute, 3700 San Martin Drive, Baltimore, MD 21218, USA; afox@stsci.edu

² Department of Physics & Astronomy, Johns Hopkins University, 3400 N. Charles St., Baltimore, MD 21218, USA

³ Space Telescope Science Institute, 3700 San Martin Drive, Baltimore, MD 21218, USA

⁴ Department of Astronomy and Astrophysics, The Pennsylvania State University, 525 Davey Laboratory, University Park, PA 16802, USA

⁵ Institute for Gravitation and the Cosmos, The Pennsylvania State University, University Park, PA 16802, USA

⁶ Institut für Physik und Astronomie, Universität Potsdam, Haus 28, Karl-Liebknecht-Str. 24/25, D-14476, Potsdam, Germany

Received 2023 February 22; revised 2023 March 14; accepted 2023 March 21; published 2023 April 5

Abstract

We present the detection of dust depletion in Complex C, a massive, infalling, low-metallicity high-velocity cloud in the northern Galactic hemisphere that traces the ongoing accretion of gas onto the Milky Way. We analyze a very high signal-to-noise Hubble Space Telescope Cosmic Origins Spectrograph spectrum of active galactic nucleus (AGN) Mrk 817 formed by coadding 165 individual exposures taken under the AGN STORM 2 program, allowing us to determine dust-depletion patterns in Complex C at unprecedented precision. By fitting Voigt components to the O I, S II, N I, Si II, Fe II, and Al II absorption and applying ionization corrections from customized CLOUDY photoionization models, we find subsolar elemental abundance ratios of $[\text{Fe}/\text{S}] = -0.42 \pm 0.08$, $[\text{Si}/\text{S}] = -0.29 \pm 0.05$, and $[\text{Al}/\text{S}] = -0.53 \pm 0.08$. These ratios indicate the depletion of Fe, Si, and Al into dust grains, since S is mostly undepleted. The detection of dust provides an important constraint on the origin of Complex C, as dust grains indicate the gas has been processed through galaxies, rather than being purely extragalactic. We also derive a low metallicity of Complex C of $[\text{S}/\text{H}] = -0.51 \pm 0.16$ ($\approx 31\%$ solar), confirming earlier results from this sight line. We discuss origin models that could explain the presence of dust in Complex C, including Galactic fountain models, tidal stripping from the Magellanic Clouds or other satellite galaxies, and precipitation of coronal gas onto dust-bearing “seed” clouds.

Unified Astronomy Thesaurus concepts: [Interstellar dust \(836\)](#); [Ultraviolet astronomy \(1736\)](#); [High-velocity clouds \(735\)](#); [Chemical abundances \(224\)](#); [Circumgalactic medium \(1879\)](#)

1. Introduction

Large-scale gas flows play essential roles in circulating mass, energy, momentum, metals, and dust grains between galaxies and their surroundings. The circulation of these basic physical quantities through galaxy halos drives and regulates galaxy evolution, with the rate of star formation ultimately controlled by the balance between the gas supply and the feedback that prevents it from collapsing into stars. Gas flows are therefore of paramount importance for galaxy evolution.

In the Milky Way (MW), we can dissect galaxy-scale gas flows in more detail than is possible in any other galaxy. Using spectroscopy, we can probe the physical, chemical, spatial, and kinematic properties of gas flows and how they distribute across the sky. Galactic inflows and outflows are typically traced via the high-velocity clouds (HVCs), clumps of multiphase gas moving too fast for Galactic rotation, in practice meaning clouds with velocities in the local standard of rest (LSR) reference frame of $|v_{\text{LSR}}| > 100 \text{ km s}^{-1}$

(Wakker & van Woerden 1997). While HVCs were discovered and first characterized in neutral gas via H I 21 cm emission, most of their mass is in ionized gas, as revealed by UV absorption-line studies (e.g., Lehner et al. 2012; Richter et al. 2017; Fox et al. 2019).

Complex C is among the best studied of all HVCs. With an infalling velocity of $v_{\text{LSR}} = -130 \text{ km s}^{-1}$ and an angular size of 1700 deg^2 in the northern Galactic hemisphere, Complex C is a poster child of accreting gas onto the Milky Way (see Figure 1). A series of UV absorption-line analyses have found a low metallicity in Complex C of $\approx 10\%$ – 30% solar (Wakker et al. 1999; Murphy et al. 2000; Gibson et al. 2001; Richter et al. 2001; Collins et al. 2003, 2007; Tripp et al. 2003; Shull et al. 2011), which point toward an extragalactic origin, though models where Complex C represents the return flow of a condensing Galactic fountain cannot be excluded (Fraternali et al. 2015). The cloud is at a distance of 10–12 kpc (Wakker et al. 2007; Thom et al. 2008), contains cold H I filaments (Marchal et al. 2021), and is surrounded by an envelope of highly ionized gas indicating an interaction with the hot Galactic halo (Fox et al. 2004).

While these earlier analyses all concluded that Complex C has a low metallicity, they did not have the sensitivity to demonstrate that Complex C contains dust grains. Dust is important because it represents a vital clue to a cloud’s origin, with Galactic clouds expected to contain dust and extragalactic clouds generally expected not to. In this Letter, we present an extremely high signal-to-noise ratio (S/N) Hubble Space Telescope Cosmic Origins Spectrograph (HST/COS) spectrum

* Based on observations made with the NASA/ESA Hubble Space Telescope, obtained from the Data Archive at the Space Telescope Science Institute, which is operated by the Association of Universities for Research in Astronomy, Inc., under NASA contract NAS5-26555. These observations are associated with program 16196.

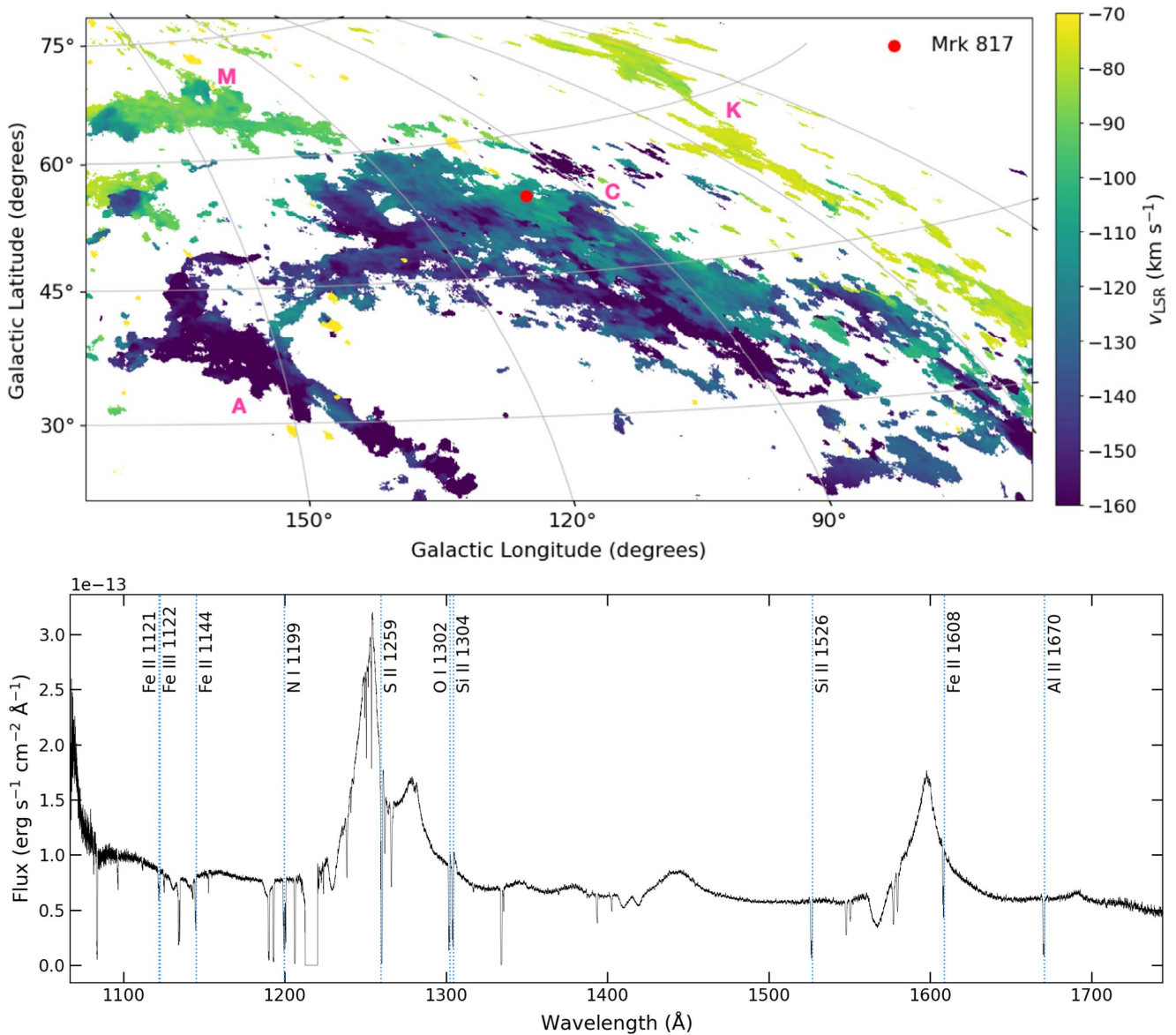


Figure 1. Top: H I 21 cm emission map of Complex C in Aitoff projection based on HI4PI data (Westmeier 2018). The map is integrated over the velocity range $-175 < v_{\text{LSR}} < -50 \text{ km s}^{-1}$. The location of Mrk 817 is marked with a red circle, and major HVC complexes are labeled in pink. Bottom: full coadded COS/FUV spectrum of Mrk 817 labeled with MW lines used in this analysis. The extremely high S/N of this spectrum enables high-precision measurements of Complex C absorption. MW Lyman-alpha absorption was not observed because the G130M/1222 grating setting places it in the gap between COS detector segments A and B.

of Mrk 817, an active galactic nucleus (AGN) lying behind Complex C, and use a UV depletion analysis to show that Complex C does contain dust, with $\approx 0.3\text{--}0.5$ dex of depletion seen in the refractory elements Si, Al, and Fe. We present our data reduction procedures in Section 2, analysis techniques in Section 3, and discussion and conclusions in Section 4.

2. Observations and Data Handling

Mrk 817 is a Seyfert 1 galaxy at $z_{\text{em}} = 0.031455$ that by good fortune lies directly behind HVC Complex C. This alignment allows a precision analysis of the cloud’s chemical composition. Mrk 817 was observed with the COS (Green et al. 2012) on board HST 165 times in a 15 month period beginning 2020 November 24 under the reverberation mapping program AGN STORM 2 (HST Program ID 16196). Each visit consisted of four 60 s exposures with G130M/1222 (one at each FP-POS position), exposures of 175 and 180 s with

G160M/1533 (at FP-POS 1 and 2, respectively), and two 195 s exposures with G160M/1577 (at FP-POS 3 and 4). All data were taken at COS far-ultraviolet (FUV) Lifetime Position 4. While the AGN STORM 2 program was designed to study the temporal variation in the continuum and line emission from the AGN itself (Kara et al. 2021), the spectra can be coadded to form a single spectrum of exquisite sensitivity, ideal for studies of the absorption in the MW halo and the foreground intergalactic medium.

The individual COS exposures were reduced using version 3.4.1 of the `calcos` data reduction pipeline. We then created two coadded spectra for use in our analysis. The first is a coadd of all 165 exposures. Full details of the coaddition steps are described in Homayouni et al. (2023). In brief, we used a Python implementation of the IRAF `splice` algorithm to resample the individual exposures onto a uniform wavelength grid before coaddition. Individual pixels were weighted by the

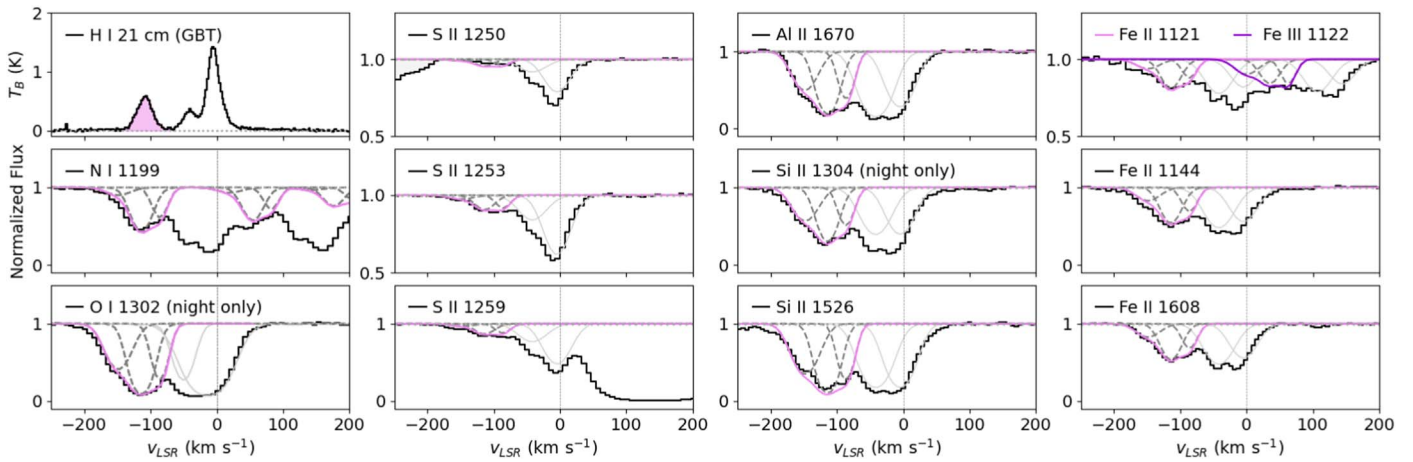


Figure 2. Voigt profile fits to the low-ion absorption from Complex C in the coadded HST/COS spectrum of Mrk 817. Normalized flux is plotted against LSR velocity for 11 low-ionization metal lines. A 21 cm spectrum from the GBT is included in the top-left panel. The Complex C components are centered at $v_{\text{LSR}} = -149, -114,$ and -86 km s^{-1} . The pink curves show the Complex C model adopted in this study. Individual components are shown with gray lines, dashed for Complex C and solid for Milky Way components. The data have been binned by 3 pixels.

exposure time in the `DQ_WGT` array. Error bars for each binned pixel were recalculated based on the total counts in each bin, assuming Poisson statistics with the low-count correction of Gehrels (1986). The second coadd was formed from the 108 spectra taken in HST orbital night time, defined as those exposures with header keyword `SUN_ALT < 20°`. This night-only spectrum minimizes geocoronal emission (airglow) from the sunlit side of the Earth’s atmosphere, which contaminates the O I $\lambda 1302$ and Si II $\lambda 1304$ lines, both key lines for our metallicity analysis.

The full coadded spectrum has an extremely high signal-to-noise ratio per pixel of 66 at 1300 \AA and 94 at 1528 \AA , corresponding to 161 and 230 per resolution element, respectively (assuming 6 pixels per resolution element). These exquisite S/N levels are possible because of the sheer number of individual exposures, the use of four FP-POS positions per grating, and the nonrepeatability in the COS mode-select mechanism, which means identical exposures fall at slightly different x -positions on the FUV detector (by up to 10 pixels). With 165 visits and four FP-POS per grating, each wavelength samples about 660 different detector locations, which greatly ameliorates pixel-level flat-field structure. The night-only spectrum has an S/N per pixel of 50 at 1300 \AA (123 per resolution element).

We applied a heliocentric-to-LSR velocity correction of 11.7 km s^{-1} , appropriate for the Galactic coordinates of Mrk 817 ($l = 100.3^\circ, b = 53.5^\circ$), using the dynamical definition of the LSR. For the reference H I column density in Complex C in the Mrk 817 direction, we use the value $\log N(\text{H I}) = 19.50 \pm 0.01$ derived by Shull et al. (2011) from a Green Bank Telescope (GBT) 21 cm spectrum taken at $9''$ angular resolution. This closely matches the value $\log N(\text{H I}) = 19.51 \pm 0.55$ obtained by summing the two Complex C components fit toward Mrk 817 by French et al. (2021) in their study of H I Lyman-series absorption.

3. UV Analysis

3.1. Voigt Profile Fitting

We used the VPFIT software package version 12.2 (Carswell & Webb 2014) to fit Voigt profiles to the MW and HVC absorption in O I $\lambda 1302$, S II $\lambda \lambda 1253, 1200.2, 1200.7$, Fe II $\lambda 1121, 1144, 1608$, Al II $\lambda 1670$, and Si II $\lambda \lambda$

1304. We focused on these six low-ionization species as they are well suited to studies of the metallicity and dust depletion in Complex C. O, S, and N are relatively undepleted (volatile) elements (Jenkins 2009), whereas Fe, Si, and Al are refractory elements that deplete onto dust grains.

For our fitting methodology, we normalized the COS spectra around each line of interest, using spline fits to regions of unabsorbed continuum. We assumed the component structure in the Milky Way and in Complex C was common to all low-ion lines under study, so we tied the line centroids and line widths for the O I, N I, S II, Si II, Fe II, and Al II fits. This assumption reflects the expected copatiality of these species given their similar ionization potentials, and allows VPFIT to solve for the column density as the one free parameter for each ion in each component. Our VPFIT models used the COS line spread function (LSF) for LP4 for the G130M/1222 and G160M/1533 settings. We fit the full profile of each ion, i.e., we include the MW (low-velocity) and Complex C (high-velocity) components in each fit.

We found evidence for three Complex C components and two MW components in all low ions under study, with a strong Complex C component at $v_{\text{LSR}} = -113.8 \pm 1.5 \text{ km s}^{-1}$ surrounded by two weaker components at $-148.6 \pm 2.5 \text{ km s}^{-1}$ and $-86.0 \pm 1.7 \text{ km s}^{-1}$. Our adopted VPFIT model to Complex C is therefore a three-component fit. This model is shown in Figure 2 and the model parameters are given in Table 1. We calculate the total column density in Complex C in each ion by summing across the three components. This is necessary because the reference H I column density in Complex C is also summed across velocity components, so integrated metal measurements are needed for a like-to-like comparison. We used VPFIT to calculate the weighted error on the total column density of each ion; this error is considerably less than the quadrature sum of the individual errors, because those errors are correlated due to degeneracies among the individual components. This allows for precise calculation of the metallicities and depletions.

3.2. CLOUDY Photoionization Models

An essential step in metallicity and dust-depletion analysis is the calculation of ionization corrections (ICs). ICs account for the amount of each ion hidden in unseen ionization stages.

Table 1
Complex C Absorption Parameters toward Mrk 817 (Three-component Models)^a

Ion	Lines Fit	$\log N_1$ (N in cm^{-2})	$\log N_2$ (N in cm^{-2})	$\log N_3$ (N in cm^{-2})	$\log N_{\text{tot}}$ (N in cm^{-2})
O I	$\lambda 1302$	14.371 ± 0.062	$>14.715^b$	14.319 ± 0.129	$15.72^{+0.24b}_{-0.16}$
S II	$\lambda 1253^c$	13.512 ± 0.162	14.017 ± 0.081	13.834 ± 0.119	14.311 ± 0.033
N I	$\lambda\lambda 1199.5, 1200.2, 1200.7$	13.048 ± 0.143	13.867 ± 0.057	13.508 ± 0.119	14.068 ± 0.013
Si II	$\lambda 1304^d$	13.912 ± 0.021	14.136 ± 0.017	13.778 ± 0.029	14.445 ± 0.009
Fe II	$\lambda\lambda 1121, 1144, 1608$	13.516 ± 0.074	13.953 ± 0.063	13.612 ± 0.126	14.213 ± 0.014
Fe III	$\lambda 1122$	13.377 ± 0.175	13.518 ± 0.134	13.388 ± 0.150	13.910 ± 0.143^e
Al II	$\lambda 1670$	12.597 ± 0.062	12.891 ± 0.068	12.520 ± 0.133	13.177 ± 0.015

Notes.

^a Our VPFIT models reveal three components within Complex C. We use the same component structure for all seven low ions, with $v_1 = -148.6 \pm 2.5 \text{ km s}^{-1}$, $b_1 = 24.6 \pm 1.8 \text{ km s}^{-1}$, $v_2 = -113.8 \pm 1.5 \text{ km s}^{-1}$, $b_2 = 20.4 \pm 2.0 \text{ km s}^{-1}$, $v_3 = -86.0 \pm 1.7 \text{ km s}^{-1}$, and $b_3 = 15.2 \pm 2.0 \text{ km s}^{-1}$. We present the column densities of each component and the total column density summed across all three. The errors on the summed totals are the weighted uncertainties from VPFIT, and are much less than the quadrature sum of the individual errors.

^b For O I $\lambda 1302$, the COS data only provide a lower limit for the total column density, because of saturation in component 2. Instead we adopt the value derived by Collins et al. (2003) from unsaturated O I absorption in Far Ultraviolet Spectroscopic Explorer data.

^c S II $\lambda 1250$ is too weak and $\lambda 1259$ is too blended to be included in the fit.

^d Si II $\lambda\lambda 1260, 1190, 1526$, and 1193 are saturated in Complex C and are not included in the fit.

^e Our error budget on $N(\text{Fe III})$ includes an additional systematic error of 0.13 dex to reflect the uncertainty in deblending the Complex C absorption in Fe III 1122 from low-velocity absorption in Fe II 1121.

They are defined as the difference between the true elemental abundance (which we seek) and the observed ion abundance (which we measure). In a photoionization model, the true abundance is known, so the IC can be calculated as

$$\text{IC}(X^i) = [X/H]_{\text{model}} - [X^i/\text{H}i], \quad (1)$$

where the square brackets denote logarithmic abundances relative to solar, i.e., $[X/H] = (\log N_X - \log N_H) - \log(X/H)_\odot$ and $[X^i/\text{H}i] = (\log N_{X^i} - \log N_{\text{H}i}) - \log(X^i/\text{H}i)_\odot$. We adopt solar (photospheric) abundances from Asplund et al. (2009), namely $\log(\text{O}/\text{H})_\odot = -3.31$, $\log(\text{S}/\text{H})_\odot = -4.88$, $\log(\text{N}/\text{H})_\odot = -4.17$, $\log(\text{Si}/\text{H})_\odot = -4.49$, $\log(\text{Fe}/\text{H})_\odot = -4.50$, and $\log(\text{Al}/\text{H})_\odot = -5.55$.

We ran customized photoionization models using the radiative transfer code CLOUDY version 22.01 (Ferland et al. 2017) to calculate the ICs in Complex C for each element under study (H, O, S, N, Si, Al, and Fe). Our modeling methodology is based on the procedures described in Cashman et al. (2023). In brief, we assume the cloud is a plane-parallel slab exposed to the 3D MW radiation field, with the spectral energy distribution taken from Fox et al. (2005) and the normalization at the distance of Complex C from Bland-Hawthorn et al. (2019). We ran a grid of models at different gas density, and found the solution that best matches the observed ratio of $\log [N(\text{Fe III})/N(\text{Fe II})] = -0.30 \pm 0.13$ in Complex C. This yielded $\log(n_{\text{H}} \text{ cm}^{-3}) = -1.47 \pm 0.13$. Alternative methods to solve for the gas density are to use the C II*/C II or Si III/Si II ratios. We cannot derive a reliable density from C II*/C II as C II $\lambda 1334$ is heavily saturated in Complex C, but the density derived from the Si III/Si II ratio is $\log(n_{\text{H}} \text{ cm}^{-3}) \approx -1.45$, very close to the density derived from Fe III/Fe II. Our derived density is close to the Complex C density of $\log(n_{\text{H}} \text{ cm}^{-3}) = -1.30$ derived by Shull et al. (2011) assuming the cloud has a similar line-of-sight depth as angular extent. We ran the CLOUDY models using the total metal column densities summed across the three Complex C components, since our H I measurement is integrated in a similar way. In principle, we could run the models on the individual components, but this would involve assumptions on how to split up the H I, so instead we present an integrated model.

The ICs are shown as a function of density for each of the ions under study in the top panel of Figure 3. Our adopted IC for each ion is calculated at the best-fit density. The IC is very small (and flat) for O I and N I (0.01–0.03 dex level), moderate for Fe II (≈ 0.15 dex level), and at the ≈ 0.20 – 0.25 dex level for Si II, S II, and Al II.

3.3. Chemical Abundances

The gas-phase abundance of element X relative to hydrogen is

$$[X/H] = [X^i/\text{H}i] + \text{IC}(X^i). \quad (2)$$

The Complex C abundances calculated with Equation (2) are shown in the middle panel of Figure 3 and listed in Table 2. For the volatile (undepleted) elements we find total abundances across the three components of $[\text{S}/\text{H}] = -0.51 \pm 0.16$, $[\text{O}/\text{H}] = -0.48^{+0.28}_{-0.22}$, and $[\text{N}/\text{H}] = -1.23 \pm 0.15$, where the errors include a 0.15 dex systematic error to account for the beam size mismatch between the UV measurements and the H I emission measurements (Wakker et al. 2011), and where the oxygen abundance uses the Collins et al. (2003) value for $N(\text{O I})$, since it is derived from unsaturated lines in the FUSE spectrum (whereas the O I $\lambda 1302$ line is saturated). These abundances agree with previous measurements along the Mrk 817 sight line (Collins et al. 2003, 2007; Shull et al. 2011) and other Complex C sightlines (Gibson et al. 2001; Richter et al. 2001; Tripp et al. 2003), and confirm that Complex C is a low-metallicity cloud with a significant nitrogen underabundance.

3.4. Dust-depletion Levels

Following convention, we define the depletion $\delta_{\text{S}}(X)$ of each refractory element X (Si, Al, or Fe) as the abundance of that element relative to sulfur:

$$\delta_{\text{S}}(X) \equiv [X/\text{S}] = [X/H] - [\text{S}/\text{H}]. \quad (3)$$

In principle, the depletions could be calculated relative to O, which has as a smaller ionization correction than S, and our results would be essentially unchanged if we did this, since our values of $[\text{S}/\text{H}]$ and $[\text{O}/\text{H}]$ are identical within their errors (see

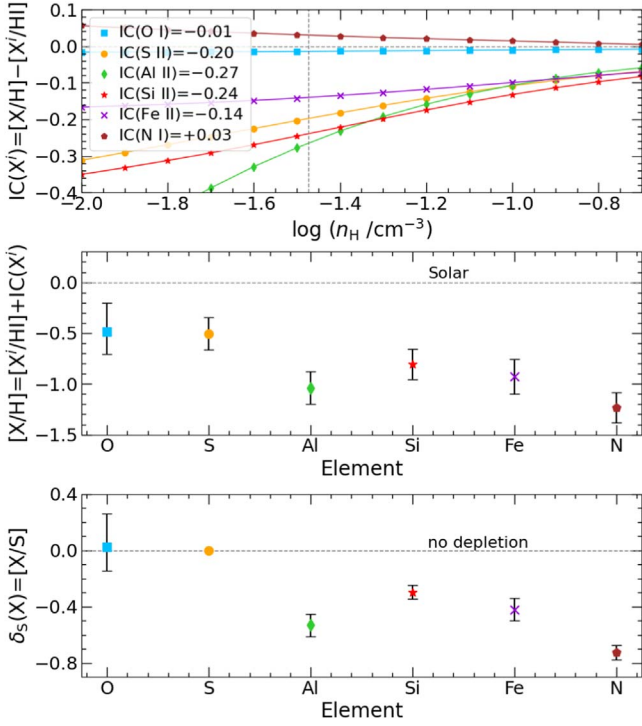


Figure 3. Derivation of elemental abundances and dust depletions in Complex C toward Mrk 817. The top panel shows the ionization corrections (ICs) from our CLOUDY models for six ions as a function of gas density. The best-fit density (dotted line) is derived by matching the observed Fe III/Fe II ratio in Complex C. The middle panel shows the ionization-corrected abundances of each element relative to hydrogen $[X/H]$. The bottom panel shows the depletion of each element relative to sulfur $[X/S]$, where S is chosen as an undepleted reference element. All data points are from our new COS analysis except oxygen, which is based on the O I measurement from Collins et al. (2003; see Table 1).

Table 2
Complex C Abundances and Depletions

Ion	$[X^i/H]$ ^a	$IC(X^i)$ ^b	$[X/H]$ ^c	$\delta_s(X)$ ^d
Volatile elements				
O I	$-0.47^{+0.28}_{-0.22}$	-0.01 ± 0.01	$-0.48^{+0.28}_{-0.22}$	$+0.03^{+0.24}_{-0.17}$
S II	-0.31 ± 0.15	-0.20 ± 0.03	-0.51 ± 0.16	...
N I	-1.26 ± 0.15	$+0.03 \pm 0.01$	-1.23 ± 0.15	-0.72 ± 0.05
Refractory elements				
Si II	-0.57 ± 0.15	-0.24 ± 0.03	-0.80 ± 0.15	-0.29 ± 0.05
Fe II	-0.79 ± 0.15	-0.14 ± 0.07	-0.93 ± 0.17	-0.42 ± 0.08
Al II	-0.77 ± 0.15	-0.27 ± 0.06	-1.04 ± 0.16	-0.53 ± 0.08

Notes.

^a Ion abundance $[X^i/H] = \log [N(X^i)/N(H I)] - \log (X/H)_\odot$, where X^i is the observed ion of element X. The error is dominated by beam-smearing uncertainties. We take the value of $\log N(H I)$ in Complex C in the Mrk 817 direction as 19.50 ± 0.01 (Shull et al. 2011).

^b Ionization correction $IC(X^i) = [X/H]_{\text{model}} - [X^i/H]$, derived from CLOUDY modeling (see Figure 3).

^c Gas-phase elemental abundance $[X/H] = [X^i/H] + IC(X^i)$.

^d Depletion of element X relative to sulfur $\delta_s(X) \equiv [X/S] = [X/H] - [S/H]$. The errors are smaller than the abundance errors because the depletions do not depend on $N(H I)$ and so do not include a beam-smearing error, but they do include the uncertainties on X^i , S II, $IC(X^i)$, and $IC(S II)$.

Table 2). However, we adopt S as the reference element as the S II column densities (derived from the high S/N COS spectrum) have much smaller error bars than the O I column

densities. The depletions for Complex C are plotted in the bottom panel of Figure 3 and presented in Table 2. Fe, Si, and Al all show similar levels of depletion, with $[Fe/S] = -0.42 \pm 0.08$, $[Si/S] = -0.29 \pm 0.05$, and $[Al/S] = -0.53 \pm 0.08$. We also derive $[N/S] = -0.72 \pm 0.05$, though this indicates an intrinsic nitrogen underabundance, not a dust effect, since N is a volatile element.

The depletions are derived purely from measurements made along a single UV sight line, and so do not depend on the beam-smearing errors that affect HVC metallicities derived from combining UV absorption with H I emission measurements made over a much larger beam. Our Complex C depletion measurements are therefore much more precise than the metallicity measurements.

4. Discussion and Conclusions

Our analysis of the UV absorption in the high-S/N coadded COS spectrum of Mrk 817 has yielded subsolar abundance ratios in Complex C of $[Fe/S] = -0.42 \pm 0.08$, $[Si/S] = -0.29 \pm 0.05$, and $[Al/S] = -0.53 \pm 0.08$. Since S is relatively undepleted but Fe, Si, and Al are known to deplete in the ISM (Savage & Sembach 1996; Jenkins 2009; Konstantopoulou et al. 2022), these ratios quantify the amount of dust depletion for Fe, Si, and Al. These are the first significant detections of dust depletion in Complex C, though limits on dust depletion were derived by Tripp (2022). As a guide, 0.5 dex of Al depletion means that only one Al atom out of three is in the gas phase, with the remaining two in dust. Similarly, two in five Fe atoms are in gas, and one in two Si atoms. The majority of the metal mass in Complex C in these three elements is therefore locked into dust grains.

It is worth considering whether other, non-dust-related effects could explain the anomalous abundance ratios derived in Complex C. In principle, nonsolar abundance ratios can be caused by nucleosynthetic effects, in which different elements have different production pathways in stars. Indeed, this is the favored explanation for the low N/S ratio (Richter et al. 2001), which is interpreted as evidence for an intrinsic underabundance of N caused by its different origin than the α -elements, rather than a dust effect, since N does not deplete (Jenkins 2009). However, for α -to- α ratios like Si/S and Si/O, the intrinsic ratio is expected to be solar, which is why the observed subsolar Si/S implies dust depletion. For the non- α elements Al and Fe, the picture is more complex, as Al is a light odd-Z element and Fe is an Fe-peak element, so we cannot rule out that their underabundance relative to S has a contribution from nucleosynthetic effects as well as from dust grains, but we follow the standard interpretation of this as a depletion effect.

The depletions of Fe, Si, and Al constitute clear evidence for dust in Complex C. The presence of dust was considered in earlier UV analyses of the Mrk 817 sight line (Collins et al. 2003, 2007; Shull et al. 2011) and the nearby sightlines to Mrk 876 (Murphy et al. 2000), PG 1259+593 (Richter et al. 2001), and 3C 351 (Tripp et al. 2003), but could not be confirmed owing to the lower S/N of the spectra available at the time. A search for thermal IR emission from dust in Complex C found a tentative detection (Miville-Deschênes et al. 2005), but this is controversial (Peek et al. 2009).

Beyond Complex C, very few detections of dust in HVCs exist in general. UV dust depletion has been reported in the Magellanic Stream (Fox et al. 2013) and its Leading Arm

(Richter et al. 2018), and the outer-arm HVC (Tripp & Song 2012; Tripp 2022), but all other UV searches for dust in HVCs have found little or no depletion (Richter et al. 2009; Richter 2017; Cashman et al. 2023). Furthermore, searches for far-IR emission from dust in HVCs have generally produced nondetections (Wakker & Boulanger 1986; Bates et al. 1988; Williams et al. 2012; Lenz et al. 2016), with the exception of a possible detection in Complex M (Peek et al. 2009).

The presence of dust in Complex C argues against a purely extragalactic origin, despite the cloud's low metallicity, because dust grains originate in stars, predominantly in AGB stars and supernovae (Ferrarotti & Gail 2006; Dwek & Cherchneff 2011). While detailed origin models for Complex C are out of the scope of this Letter, a successful model must now simultaneously explain the cloud's low metallicity and moderate dust depletion. This combination could be explained by a "polluted accretion" model where an infalling extragalactic cloud is enriched by Galactic dust grains. However, it is also consistent with a fountain-driven circulation model (Fraternali et al. 2015; Fraternali 2017), in which a dust-bearing cloud originating in the Galactic disk was driven into the halo and precipitated the cooling of the (lower metallicity) hot corona via thermal instabilities (see also Maller & Bullock 2004; Heitsch et al. 2022; Marasco et al. 2022). In either of these models, Complex C is neither purely Galactic nor purely extragalactic, but a combination of the two. Another possible origin is tidally stripped gas from satellite galaxies, such as the Magellanic Clouds, which could potentially explain the low metallicity and the presence of dust. In any of these scenarios, the gaseous assembly history of the Milky Way is complex, with gas flows exchanging metals and dust grains in the circumgalactic medium.

In closing, our results in this Letter illustrate how very-high-S/N UV spectroscopy of AGN enables high-precision measurements of MW halo clouds. Such deep UV spectroscopy offers a range of scientific benefits.

We thank the referee for a constructive report. Support for program 16196 was provided by NASA through a grant from the Space Telescope Science Institute, which is operated by the Association of Universities for Research in Astronomy, Inc., under NASA contract NAS5-26555. The COS data are available at doi:10.17909/n734-k698.

Facility: HST/COS (Green et al. 2012).

Software: VPFIT (Carswell & Webb 2014), CLOUDY (Ferland et al. 2017).

ORCID iDs

Andrew J. Fox  <https://orcid.org/0000-0003-0724-4115>

Frances H. Cashman  <https://orcid.org/0000-0003-4237-3553>

Gerard A. Kriss  <https://orcid.org/0000-0002-2180-8266>

Gisella de Rosa  <https://orcid.org/0000-0003-3242-7052>

Rachel Plesha  <https://orcid.org/0000-0002-2509-3878>

Yasaman Homayouni  <https://orcid.org/0000-0002-0957-7151>

Philipp Richter  <https://orcid.org/0000-0002-1188-1435>

References

- Asplund, M., Grevesse, N., Sauval, A. J., & Scott, P. 2009, *ARA&A*, 47, 481
- Bates, B., Catney, M. G., & Keenan, F. P. 1988, *Ap&SS*, 146, 195
- Bland-Hawthorn, J., Maloney, P. R., Sutherland, R., et al. 2019, *ApJ*, 886, 45
- Carswell, R. F., & Webb, J. K. 2014, VPFIT: Voigt profile fitting program, Astrophysics Source Code Library, ascl:1408.015
- Cashman, F. H., Fox, A. J., Wakker, B. P., et al. 2023, *ApJ*, 944, 65
- Collins, J. A., Shull, J. M., & Giroux, M. L. 2003, *ApJ*, 585, 336
- Collins, J. A., Shull, J. M., & Giroux, M. L. 2007, *ApJ*, 657, 271
- Dwek, E., & Cherchneff, I. 2011, *ApJ*, 727, 63
- Ferland, G. J., Chatzikos, M., Guzmán, F., et al. 2017, *RMxAA*, 53, 385
- Ferrarotti, A. S., & Gail, H. P. 2006, *A&A*, 447, 553
- Fox, A. J., Richter, P., Ashley, T., et al. 2019, *ApJ*, 884, 53
- Fox, A. J., Richter, P., Wakker, B. P., et al. 2013, *ApJ*, 772, 110
- Fox, A. J., Savage, B. D., Wakker, B. P., et al. 2004, *ApJ*, 602, 738
- Fox, A. J., Wakker, B. P., Savage, B. D., et al. 2005, *ApJ*, 630, 332
- Fraternali, F. 2017, in *Astrophysics and Space Science Library, Gas Accretion onto Galaxies*, ed. A. Fox & R. Davé, Vol. 430 (Berlin: Springer), 323
- Fraternali, F., Marasco, A., Armillotta, L., & Marinacci, F. 2015, *MNRAS*, 447, L70
- French, D. M., Fox, A. J., Wakker, B. P., et al. 2021, *ApJ*, 923, 50
- Gehrels, N. 1986, *ApJ*, 303, 336
- Gibson, B. K., Giroux, M. L., Penton, S. V., et al. 2001, *AJ*, 122, 3280
- Green, J. C., Froning, C. S., Osterman, S., et al. 2012, *ApJ*, 744, 60
- Heitsch, F., Marchal, A., Miville-Deschênes, M. A., Shull, J. M., & Fox, A. J. 2022, *MNRAS*, 509, 4515
- Homayouni, Y., De Rosa, G., Plesha, R., et al. 2023, arXiv:2302.11587
- Jenkins, E. B. 2009, *ApJ*, 700, 1299
- Kara, E., Mehdipour, M., Kriss, G. A., et al. 2021, *ApJ*, 922, 151
- Konstantopoulou, C., De Cia, A., Krogager, J.-K., et al. 2022, *A&A*, 666, A12
- Lehner, N., Howk, J. C., Thom, C., et al. 2012, *MNRAS*, 424, 2896
- Lenz, D., Flöer, L., & Kerp, J. 2016, *A&A*, 586, A121
- Maller, A. H., & Bullock, J. S. 2004, *MNRAS*, 355, 694
- Marasco, A., Fraternali, F., Lehner, N., & Howk, J. C. 2022, *MNRAS*, 515, 4176
- Marchal, A., Martin, P. G., & Gong, M. 2021, *ApJ*, 921, 11
- Miville-Deschênes, M. A., Boulanger, F., Reach, W. T., & Noriega-Crespo, A. 2005, *ApJL*, 631, L57
- Murphy, E. M., Sembach, K. R., Gibson, B. K., et al. 2000, *ApJL*, 538, L35
- Peek, J. E. G., Heiles, C., Putman, M. E., & Douglas, K. 2009, *ApJ*, 692, 827
- Richter, P. 2017, in *Astrophysics and Space Science Library, Gas Accretion onto Galaxies*, ed. A. Fox & R. Davé, Vol. 430 (Berlin: Springer), 15
- Richter, P., Charlton, J. C., Fangano, A. P. M., Bekhti, N. B., & Masiero, J. R. 2009, *ApJ*, 695, 1631
- Richter, P., Fox, A. J., Wakker, B. P., et al. 2018, *ApJ*, 865, 145
- Richter, P., Nuza, S. E., Fox, A. J., et al. 2017, *A&A*, 607, A48
- Richter, P., Sembach, K. R., Wakker, B. P., et al. 2001, *ApJ*, 559, 318
- Savage, B. D., & Sembach, K. R. 1996, *ARA&A*, 34, 279
- Shull, J. M., Stevans, M., Danforth, C., et al. 2011, *ApJ*, 739, 105
- Thom, C., Peek, J. E. G., Putman, M. E., et al. 2008, *ApJ*, 684, 364
- Tripp, T. M. 2022, *MNRAS*, 511, 1714
- Tripp, T. M., & Song, L. 2012, *ApJ*, 746, 173
- Tripp, T. M., Wakker, B. P., Jenkins, E. B., et al. 2003, *AJ*, 125, 3122
- Wakker, B. P., & Boulanger, F. 1986, *A&A*, 170, 84
- Wakker, B. P., Howk, J. C., Savage, B. D., et al. 1999, *Natur*, 402, 388
- Wakker, B. P., Lockman, F. J., & Brown, J. M. 2011, *ApJ*, 728, 159
- Wakker, B. P., & van Woerden, H. 1997, *ARA&A*, 35, 217
- Wakker, B. P., York, D. G., Howk, J. C., et al. 2007, *ApJL*, 670, L113
- Westmeier, T. 2018, *MNRAS*, 474, 289
- Williams, R. J., Mathur, S., Poindexter, S., Elvis, M., & Nicastro, F. 2012, *AJ*, 143, 82